JGR Atmospheres

RESEARCH ARTICLE
10.1029/2021JD034908

Special Section:
Fire in the Earth System

Impacts of Biomass Burning in Peninsular Southeast Asia on $PM_{2.5}$ Concentration and Ozone Formation in Southern China During Springtime—A Case Study

Li Xing[1,2], Naifang Bei[3], Jianping Guo[4], Qiyuan Wang[2,5], Suixin Liu[2,5], Yongming Han[2,5], Siwatt Pongpiachan[6], and Guohui Li[2,5]

[1]School of Geography and Tourism, Shaanxi Normal University, Xi'an, China, [2]SKLLQG, Institute of Earth Environment, Chinese Academy of Sciences, Xi'an, China, [3]School of Human Settlements and Civil Engineering, Xi'an Jiaotong University, Xi'an, China, [4]State Key Laboratory of Severe Weather, Chinese Academy of Meteorological Sciences, Beijing, China, [5]CAS Center for Excellence in Quaternary Science and Global Change, Xi'an, China, [6]School of Social and Environmental Development, National Institute of Development Administration, Bangkok, Thailand

Key Points:

- Biomass burning in peninsular Southeast Asia (BB-PSEA) significantly increase near-surface $PM_{2.5}$ concentrations in southern China
- NH_3 emissions from BB-PSEA play a key role in the enhancement of secondary inorganic aerosols in southern China
- The aerosol-radiation and aerosol-photolysis interactions from BB-PSEA decrease O_3 concentrations in southern China

Supporting Information:

Supporting Information may be found in the online version of this article.

Correspondence to:

G. Li,
ligh@ieecas.cn

Citation:

Xing, L., Bei, N., Guo, J., Wang, Q., Liu, S., Han, Y., et al. (2021). Impacts of biomass burning in peninsular Southeast Asia on $PM_{2.5}$ concentration and ozone formation in southern China during springtime—A case study. *Journal of Geophysical Research: Atmospheres*, *126*, e2021JD034908. https://doi.org/10.1029/2021JD034908

Received 12 MAR 2021
Accepted 25 OCT 2021

Abstract Biomass burning (BB) affects fine particulate matter ($PM_{2.5}$) concentration and ozone (O_3) formation by emitting gaseous precursors and primary aerosols. The Impacts of BB in peninsular Southeast Asia (BB-PSEA) on $PM_{2.5}$ concentration and O_3 formation in southern China are evaluated using a source-oriented WRF-Chem model to simulate an air pollution episode from March 21 to March 25, 2015. The source-oriented model separates the emissions from BB-PSEA and other sources and can evaluate the effects of aerosol-radiation interactions (ARIs) and aerosol-photolysis interactions (APIs) from BB-PSEA. Comparisons with observations reveal that the model performs well in simulating the air pollution episode. Sensitivity experiments show that BB-PSEA increases $PM_{2.5}$ concentrations on the regional average by 39.3 $\mu g\ m^{-3}$ (68.0%) in Yunnan Province (YNP) and 8.4 $\mu g\ m^{-3}$ (24.1%) in other downwind areas (ODAs) in southern China, including the provinces of Guizhou, Guangxi, Hunan, Guangdong, Jiangxi, Fujian, and Zhejiang. $PM_{2.5}$ enhancement is mainly attributed to primary aerosols in YNP and to secondary aerosols in ODA. BB-PSEA increases O_3 concentrations by 18.1 $\mu g\ m^{-3}$ (19.4%) in YNP and decreases O_3 concentrations by 3.7 $\mu g\ m^{-3}$ (5.3%) in ODA. The O_3 increase in YNP is attributed to the gaseous emissions of BB-PSEA, and the O_3 decrease in ODA is caused by the effects of ARI and API from BB-PSEA. NH_3 emissions from BB-PSEA play a key role in enhancing secondary inorganic aerosols in southern China and determining increases in $PM_{2.5}$ concentrations in ODA.

1. Introduction

Biomass burning (BB) emits abundant trace gases and aerosols, affecting not only air quality by involving atmospheric photochemistry and aerosol-photolysis interactions (API), but also regional weather and climate by aerosol-radiation interactions (ARIs) and aerosol-cloud interactions (ACI) over source and downwind areas (Ajoku et al., 2021; Booth et al., 2012; Guo et al., 2016; Li et al., 2016; L. Liu et al., 2020). Intense BB occurs frequently in spring in peninsular Southeast Asia (including Myanmar, Thailand, Laos, Vietnam, and Cambodia, hereafter referred to as PSEA) because of slash-and-burn and land-clearing practices before the local growing season, the start date of which ranges from March to May (Fox et al., 2009; Jian & Fu, 2014; Suepa et al., 2016).

BB-emitted aerosols are dominated by black and organic carbon (Cui et al., 2018). They contribute 41% and 74% to the total primary black carbon and organic carbon emissions globally, respectively (Bond et al., 2004), and constitute an important source of fine particulate matter ($PM_{2.5}$) in both source and downwind areas (Fu et al., 2012; G. Li et al., 2017; J. Li et al., 2017; M. Li et al., 2017). However, BB emissions have a complicated influence on tropospheric ozone (O_3), which is formed as a result of photochemical reactions involving volatile organic compounds (VOCs)/CO and nitrogen oxide (NO_x) in the presence of sunlight (Brasseur et al., 1999). As precursors, BB-emitted VOCs/CO and NO_x are directly involved in the photochemical production processes of tropospheric O_3 (Jiang et al., 2012; M. Li et al., 2018; L. Zhang et al., 2014). BB-emitted aerosols provide surfaces for heterogeneous reactions of O_3 and radicals, causing a decrease in O_3 concentrations (M. Li et al., 2018). Carbonaceous aerosols emitted by BB efficiently absorb incoming solar ultraviolet radiation, reducing the photolysis rate and suppressing O_3 formation (Jiang et al., 2012; Li et al., 2005;

Li, Bei, et al., 2011). In addition, the induced ARI and ACI effects of BB aerosols influence the atmospheric thermodynamic and dynamic fields, disturbing O_3 photochemistry in source and downwind areas (Jiang et al., 2012; Li et al., 2018; Wu et al., 2019). Wu et al. (2019) revealed that ARI attenuates near-surface solar radiation by aerosol absorption and/or scattering, which decreases the near-surface temperature, suppresses the planetary boundary layer (PBL) height (PBLH), reduces near-surface wind speed, and consequently deteriorates the haze pollution in the North China Plain.

In spring, the prevailing westerly wind brings gaseous and particulate pollutants emitted from BB in PSEA (BB-PSEA) to southern China, affecting $PM_{2.5}$ concentrations and O_3 photochemistry in the area. BB from Burma and Northeast India can affect aerosol optical properties in Kunming, Yunnan Province (YNP), southern China and contribute approximately 57% of the total aerosol optical depth (AOD) in Kunming during March and April (J. Zhu et al., 2016, 2017). Simulations by G. Li et al. (2017), J. Li et al. (2017), and M. Li et al. (2017) have shown that BB-PSEA contributes 10%–40% of near-surface $PM_{2.5}$ concentrations in southwestern China. Using the regional CMAQ model, Fu et al. (2012) found that the long-range transport of air pollutants from BB-PSEA increases $PM_{2.5}$ and O_3 concentrations by 20%–70% and 10%–30%, respectively, in southern China, particularly in YNP and Guangxi Province near the source region. However, Deng et al. (2008) reported that observed O_3 concentrations in the Pearl River Delta (PRD) in China under the influence of BB-PSEA in March 2006 are lower than those without the impact of BB-PSEA.

Notably, the CMAQ model results of increased O_3 concentrations in southern China because of BB-PSEA are inconsistent with observations in the PRD by Deng et al. (2008). The CMAQ model used by Fu et al. (2012) is in the off-line mode and did not consider API and ARI, which may cause inconsistency in the BB-PSEA effect on O_3 concentrations in southern China. Aerosols aloft can absorb or scatter incoming solar radiation, attenuate near-surface radiation intensity, and therefore reduce gaseous photolysis rates. Li et al. (2005) have shown that black carbon reduces the photolysis rates of $O(^1d)$ and NO_2 by 10%–30% and decreases near-surface O_3 concentrations by 5%–20% in Houston and its surrounding areas. API has been reported to reduce near-surface daytime O_3 concentrations by 2%–17% in the urban areas of Mexico City, mainly because of black carbon and organic aerosols (Li, Bei, et al., 2011). Wu et al. (2020) have shown that API decreases near-surface O_3 concentrations and $PM_{2.5}$ concentrations by approximately 18.6% and 4.2%, respectively, in the North China Plain during a wintertime haze episode. M. Li et al. (2018) have indicated that O_3 precursors emitted by the agricultural fire in the Yangtze River Delta are the most important factors affecting local O_3 photochemistry, and the induced ARI only decreases the near-surface O_3 mixing ratio by 1% in the smoke plume. Jiang et al. (2012) have also reported that that the O_3 increase due to gaseous precursors emitted by BB exceeds the O_3 decrease caused by the BB-induced ARI in the western United States. In southern China, there is still a lack of comprehensive studies quantifying the effects of aerosols and gaseous emissions from BB-PSEA on O_3 photochemistry.

Considering the lack of comprehensive studies examining the effects of ARI and API as well as the gaseous emissions from BB-PSEA on $PM_{2.5}$ and O_3 concentrations in southern China, this study aims to evaluate the contribution of BB-PSEA to near-surface $PM_{2.5}$ and O_3 concentrations in southern China using a source-oriented WRF-Chem model. The model configuration and data used in this study are described in Section 2. Section 3 presents the model performance validation and results. The conclusions are summarized in Section 4.

2. Data and Model Configuration

2.1. WRF-Chem Model and Configurations

Here, a source-oriented version of the WRF-Chem model is used to evaluate the effects of emissions from BB-PSEA on air quality in southern China. The model is originally developed by Grell et al. (2005) and further modified by G. Li et al. (2010), Li, Bei, et al. (2011), Li, Zavala, et al. (2011), Li et al. (2012) and Wu et al. (2020). Both the chemical and meteorological components follow the mass and scalar conservation of the transport mechanism. The model uses the SAPRC-99 gas-phase chemical mechanism and aerosol module in CMAQ/Models3 (Binkowski & Roselle, 2003). Aerosols are represented by three log-normal distribution functions, and particle nucleation, coagulation, and size evolution are simulated in the model. Inorganic aerosols are predicted by ISORROPIA version 1.7 (Nenes et al., 1998). The organic aerosol module is

based on the volatility bases set approach with the aging of primary organic aerosols and the heterogeneous reactions of glyoxal and methylglyoxal, as described previously (Li, Zavala, et al., 2011). The dry and wet deposition of chemical species use the parameterization of Wesely (1989) and the method in the CMAQ module, respectively.

The air pollutants emitted by BB-PSEA are marked as SPECIES_B and those from other sources as SPECIES_A. SPECIES_A and SPECIES_B are tracked independently in chemical, physical, and dynamic processes in the model simulation. For example, nitrate formation from the gas phase reaction of NO_2 with the hydroxyl radical (OH) in the original WRF-Chem model is described as follows:

$$NO_2 + OH \rightarrow HNO_3(g) \leftrightarrow NO_3^- \quad (1)$$

where $HNO_3(g)$ and NO_3^- denote gas-phase nitric acid and particulate nitrate, respectively. In the source-oriented WRF-Chem model, NO_2 from BB-PSEA and other sources are denoted as NO_2_B and NO_2_A, respectively. Equation 1 is expressed as:

$$NO_2\_A + OH \rightarrow HNO_3(g)\_A \leftrightarrow NO_3^-\_A \quad (2)$$

$$NO_2\_B + OH \rightarrow HNO_3(g)\_B \leftrightarrow NO_3^-\_B \quad (3)$$

Thus, the source-oriented model could separately track nitrate formation contributed by BB-PSEA and other sources. Notably, O_3 contributed by different sources in the model is not tagged, although other studies could tag ozone from different sources (Wang et al., 2011).

To evaluate the effects of ARI and API that were induced by BB-PSEA on $PM_{2.5}$ concentrations and O_3 photochemistry, the Goddard shortwave radiation module (Chou & Suarez, 1999; Chou et al., 2001) and the Fast Tropospheric Ultraviolet and Visible (FTUV) Radiation Model (Li et al., 2005; Tie et al., 2003) are revised according to the chemical species of the source-oriented WRF-Chem model. An aerosol radiative module developed by Li, Bei, et al. (2011) is used to calculate the aerosol optical properties, including AOD, single scattering albedo, and asymmetry factor. The calculated aerosol optical properties are transferred into the Goddard shortwave radiation module to evaluate ARI effects and the FTUV radiation model to evaluate API effects (Wu et al., 2020). Aerosol-cloud interactions are not considered in this study.

To evaluate the impact of BB-PSEA on $PM_{2.5}$ and O_3 concentrations in southern China, the source-oriented WRF-Chem model is used to simulate an air pollution episode from March 21 to March 25, 2015. The model is configured with a horizontal grid resolution of 9 km and 35 vertical layers. The model domain includes 420 × 420 grid cells centered at 20°N and 105°E (Figure 1). The microphysical parameterization scheme developed by Hong and Lim (2006), the MYJ TKE planetary boundary layer scheme (Janjić, 2002), the MYJ surface layer scheme (Janjić, 2002), and the Unified Noah land-surface model (Chen & Dudhia, 2001) are chosen for the simulations. The chemical initial and boundary conditions use the model output from the Model for OZone And Related chemical Tracers at 6 h intervals (Horowitz et al., 2003), including anthropogenic emissions, BB, biogenic emissions, and oceanic sources. The spin-up time for the simulation is 2 days.

The anthropogenic emission inventory MIX developed by G. Li et al. (2017), J. Li et al. (2017), and M. Li et al. (2017) for East Asia is used in the simulation. The MIX inventory includes emission sectors of agriculture, industry, power plants, residential living, and transportation, with horizontal resolution of 0.25° × 0.25° and the base year of 2010. The MIX emissions are re-gridded to the grid cells in the simulations. In addition, the anthropogenic emissions in China are updated using the Multi-resolution Emission Inventory for China with the base year of 2015 (Zheng et al., 2018). Biogenic emissions are calculated using the Model of Emissions of Gases and Aerosols from Nature (Guenther et al., 2006).

2.2. BB Emissions

The emissions of air pollutants from BB-PSEA are taken from the Fire Inventory from NCAR (FINN; Wiedinmyer et al., 2006, 2011). The FINN provides daily high-resolution (1 km) open BB emissions based on the satellite observations of active fires and land cover, combined with the emission factors and estimated fuel loadings. The FINN inventory has been widely used in chemical transport models, but lacks the vertical

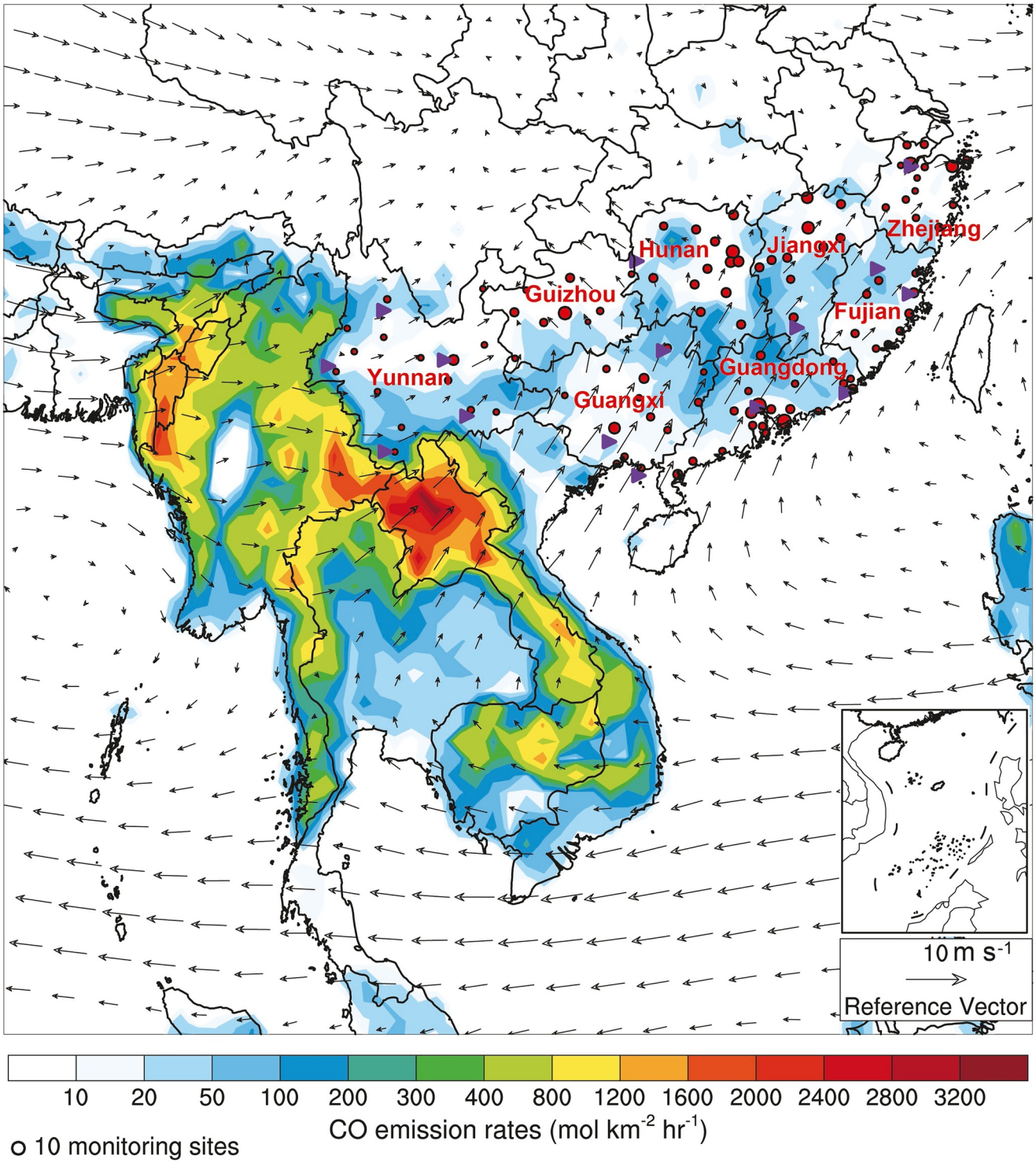

Figure 1. Model simulation domain with the mean CO emission rates in March and April during 2013–2016 and the corresponding wind field at 850 hPa from ERA-interim data set. Red dots denote centers of cities with ambient monitoring sites for air pollutants in eight provinces of southern China and the sizes of circles denote the number of ambient monitoring sites of cities. Purple triangles denote monitoring sites with the measurement of downward solar radiation. The red texts represent eight provinces of Yunnan, Guizhou, Guangxi, Hunan, Guangdong, Jiangxi, Fujian, and Zhejiang in southern China.

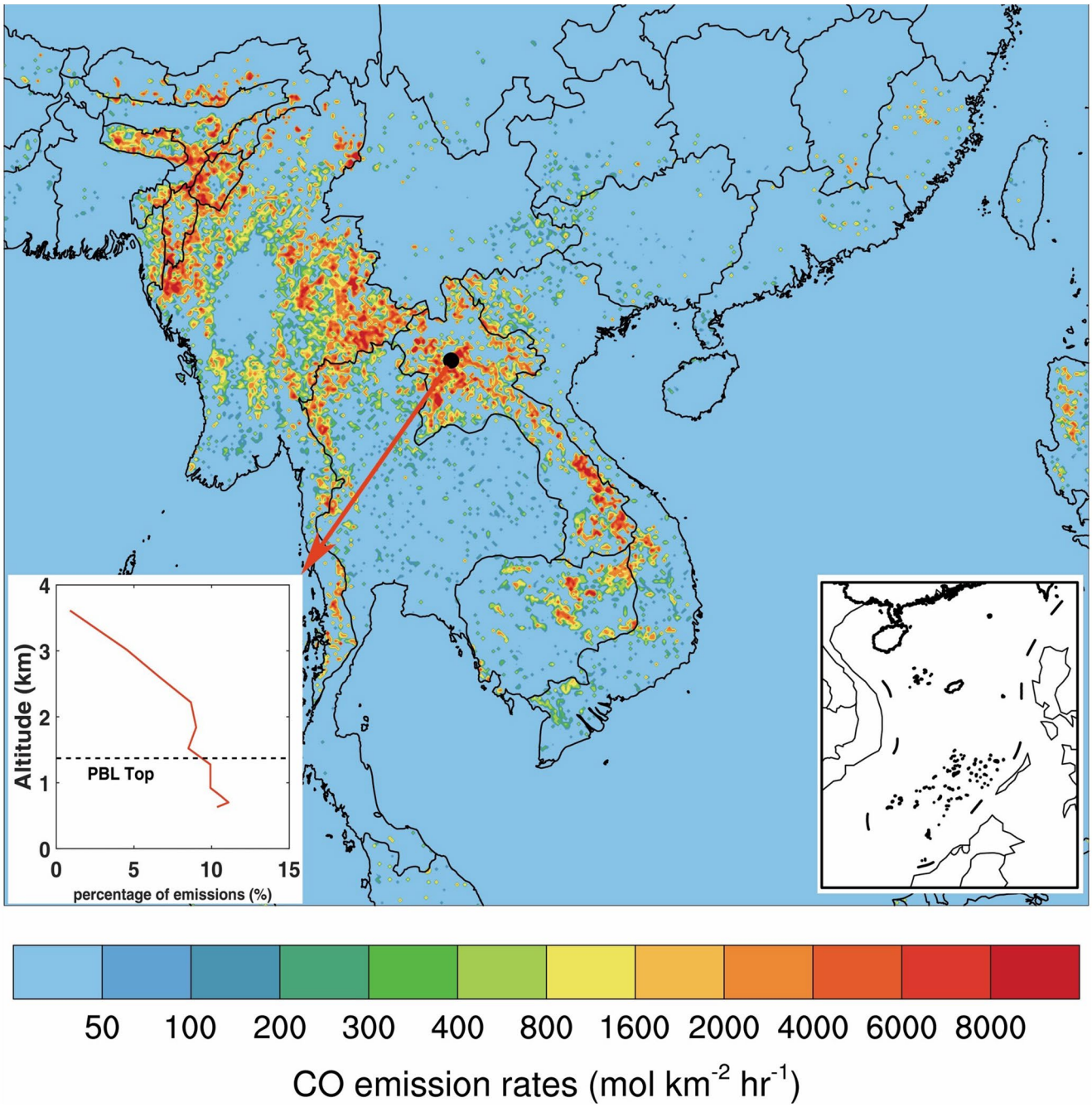

Figure 2. Horizontal distribution of mean CO emission rates from March 21 to 25, 2015, and the vertical percentage distribution of the CO emissions for an example site at 20°N and 102°E in Laos.

distribution of emissions. Notably, the BB emissions from the FINN inventory are higher than those from the Global Fire Emissions Database (L. Liu et al., 2020; T. Liu, et al., 2020). The injection height of BB plumes can reach above the PBL and significantly influence air quality in downwind areas (Jian & Fu, 2014; Zhu et al., 2018). Zhu et al. (2018) developed a new BB emission injection height scheme based on monthly gridded Multi-angle Imaging SpectroRadiometer global plume-height stereoscopic observations in 2008 and provided the vertical distribution of BB emissions with a 2.5° × 2.5° horizontal grid for each season. Here, the vertical distribution of BB plumes developed by Zhu et al. (2018) is employed and the distribution to our model is re-gridded vertically and horizontally. Figure 2 shows BB CO emissions averaged during the

simulation period and the vertical distribution of BB plumes for one example location at 20°N and 102°E in Laos. During the simulation period, BB occurs intensively in Myanmar, northwestern Thailand, Laos, and northern Cambodia. It also occurs in southern China, but the emission intensity and domain are significantly lower than those in the PSEA. The BB plumes at 20°N and 102°E in Laos reach up to 3.6 km, and 39% of the BB emissions are emitted above the PBL and transported further to the downwind areas.

2.3. Reanalysis Data

The FINN inventory monthly average BB emissions in March and April from 2013 to 2016 in Southeast Asia and the corresponding monthly mean horizontal wind field at 850 hPa, with a horizontal resolution of 0.125° × 0.125° from the ERA-interim data set (https://apps.ecmwf.int/datasets/data/interim-full-mnth/levtype=pl/), are used to characterize the transport of BB-PSEA emissions. The Terra- and Aqua- Moderate Resolution Imaging Spectroradiometer (MODIS) level 2 products of MOD04_L2.061 and MYD04_L2.061 (Levy et al., 2017) are used to obtain the daily AOD with a horizontal resolution of 0.1° × 0.1° at nadir.

2.4. Observation Data

The hourly measurements for $PM_{2.5}$, NO_2, CO, and O_3 concentrations released by China's Ministry of Ecology and Environment (http://www.cnemc.cn/sssj/) in eight provinces of southern China (Yunnan, Guangxi, Guizhou, Guangdong, Hunan, Fujian, Jiangxi, and Zhejiang; Figure 1) are used to validate the model performance of $PM_{2.5}$, NO_2, CO, and O_3. The hourly downward shortwave flux (SWDOWN) at 15 sites (Figure 1) from the China Meteorological Administration are used to evaluate the model performance of radiation and underwent quality assurance/quality control before being released to the public.

2.5. Statistical Methods for Comparisons

The mean bias (MB), root mean square error (RMSE), and index of agreement (IOA) are used to evaluate the model prediction of chemical species, and are expressed as follows:

$$\mathrm{MB} = \frac{1}{N}\sum_{i=1}^{N}\left(P_i - O_i\right) \tag{4}$$

$$\mathrm{RMSE} = \left[\frac{1}{N}\sum_{i=1}^{N}\left(P_i - O_i\right)^2\right]^{\frac{1}{2}} \tag{5}$$

$$\mathrm{IOA} = 1 - \frac{\sum_{i=1}^{N}\left(P_i - O_i\right)^2}{\sum_{i=1}^{N}\left(\left|P_i - \bar{O}\right| + \left|O_i - \bar{O}\right|\right)^2} \tag{6}$$

where P_i and O_i are the predicted and observed concentrations of chemical species, respectively. For each observation site at a certain time, P_i is extracted from the simulated concentration of species i at the model grid nearest to the location of the site, and compared with O_i at that time. N is the number of model and observation data used for comparisons and $\bar{O}$ is the average concentration of observations. The IOA ranges from 0 to 1, and one indicates perfect agreement between the model and the observation.

2.6. Numerical Model Experiments

To evaluate the contributions of emissions from BB-PSEA to $PM_{2.5}$ and O_3 concentrations in southern China, six numerical experiments are designed (Table 1). The BASE experiment includes both aerosol and gas emissions from BB-PSEA and the anthropogenic and biogenic sources in the simulation domain, considering both ARI and API. All sensitivity experiments are based on the BASE case. The BB0 experiment excludes emissions from BB-PSEA. The BB_ARI0, BB_API0, and BB_ARI&API0 experiments exclude the ARI, API, and the both caused by aerosols from BB-PSEA, respectively. The BB_GAS experiment only considers gaseous emissions from BB-PSEA.

Table 1
Summary of Numerical Model Experiments and Definitions of the Various Contribution of Aerosol and Gas Emissions From Biomass Burning in PSEA

Case	All emissions except BB-PSEA (A)	BB-PSEA aerosol emissions (B)	BB-PSEA gas emissions (B)	ARI	API
BASE[a]	√	√	√	A + B	A + B
BB0[b]	√	×	×	A	A
BB_ARI0[c]	√	√	√	A	A + B
BB_API0[d]	√	√	√	A + B	A
BB_ARI&API0[e]	√	√	√	A	A
BB_GAS[f]	√	×	√	A + B	A + B

[a]BASE represents the simulation including all emissions, and the API and ARI effects of all emissions. [b]BB0 represents the simulation excluding the BB-PSEA emission and without the API and ARI effects of BB-PSEA. [c]BB_ARI0 is the same as the BASE case, but without the ARI effect of BB-PSEA. [d]BB_API0 is the same as the BASE case, but without the API effect of BB-PSEA. [e]BB_ARI&API0 is the same as the BASE case, but without the ARI and API effects of BB-PSEA. [f]BB_GAS represents the simulation excluding the aerosol emissions from BB-PSEA.

The brute force method (BFM) is used to evaluate the contribution of BB-PSEA emissions to $PM_{2.5}$ and O_3 concentrations in southern China (Marmur et al., 2005). For example, total $PM_{2.5}$ and O_3 contributions are quantified by differentiating the results of BASE and BB0 cases. Notably, the BFM has limitations in evaluating the source contribution because the complicated non-linear interaction between various sources and the ARI and API effects induced by the source are not considered (Zhang & Ying, 2011).

3. Results and Discussions

Figure 1 indicates the spatial distribution of average BB CO emissions during springtime in March and April from 2013 to 2016 from the FINN inventory and the corresponding horizontal wind field at 850 hPa. The high BB CO emissions are concentrated in northern Laos, Eastern Myanmar, and Eastern India, exceeding 2,000 mol km^{-2} h^{-1}. The prevailing westerly and southwesterly winds in Southeast Asia are subject to bringing BB-PSEA plumes to southern China, affecting $PM_{2.5}$ concentrations and O_3 photochemistry in the area. For convenience of our analysis, we divide southern China affected by the BB-PSEA into two parts: YNP, which is adjacent to the BB source area, and the other downwind areas (ODAs), including provinces such as Guangdong, Guangxi, Guizhou, Hunan, Fujian, Jiangxi, and Zhejiang.

3.1. Model Performance

Figure 3 shows the time series of the simulated and observed near-surface CO, NO_2, O_3, and $PM_{2.5}$ concentrations averaged at the observation sites in eight provinces of southern China during the episode. The model generally reproduces the observed temporal evolution of the gaseous pollutants of CO, NO_2, and O_3 well, with IOAs exceeding 0.75. Compared with the observations, the model slightly underestimates CO, NO_2, and O_3 concentrations, with MBs of −19.7, −0.6, and −0.9 μg m^{-3}, respectively. The RMSEs of simulated O_3, CO, and NO_2 are 9.7, 132.5, and 6.6 μg m^{-3}, respectively, which are relatively small, showing less dispersion of simulations against observations. The simulated average $PM_{2.5}$ concentrations show less fluctuations during the episode, which is generally consistent with the observations, with an IOA of 0.82. The model slightly overestimates the $PM_{2.5}$ concentrations but the dispersion is considerable, with an MB and RMSE of 3.0 and 8.3 μg m^{-3}, respectively.

Figure S1 in Supporting Information S1 presents the comparison between the simulated and observed near-surface CO, NO_2, O_3, and $PM_{2.5}$ concentrations for all monitoring sites in Figure 1 averaged during the simulation period. The model generally reproduces the spatial distribution of $PM_{2.5}$, CO, NO_2, and O_3 compared with observations in southern China, and the correlation coefficients between the simulated and observed CO, NO_2, O_3, and $PM_{2.5}$ concentrations range from 0.38 to 0.65 ($p < 0.01$). The average simulated AOD with the MODIS retrieval during the simulation period was further compared (Figure S2 in Supporting Information S1). The MODIS-retrieved AOD is higher than 1.2 at the junction of Myanmar, Thailand, Laos, China, northwestern Myanmar, and southeast Thailand. The model generally reproduces the spatial distribution of AOD against the MODIS retrieval, but overestimates AOD in Myanmar, central Laos, southern China, and northwestern Myanmar, and underestimates AOD in Cambodia, Vietnam, and at the junction of Myanmar, Laos, and Thailand.

Figure 4 indicates the diurnal variations of the average simulated and observed SWDOWN at the 15 observation sites in eight provinces of southern China. The model captures the diurnal profiles of SWDOWN well, with an IOA and RSME of 0.98 and 62.1 W m^{-2}, respectively. The model overestimates the SWDOWN, with an MB of 27.2 W m^{-2}, which is caused by the noontime overestimation.

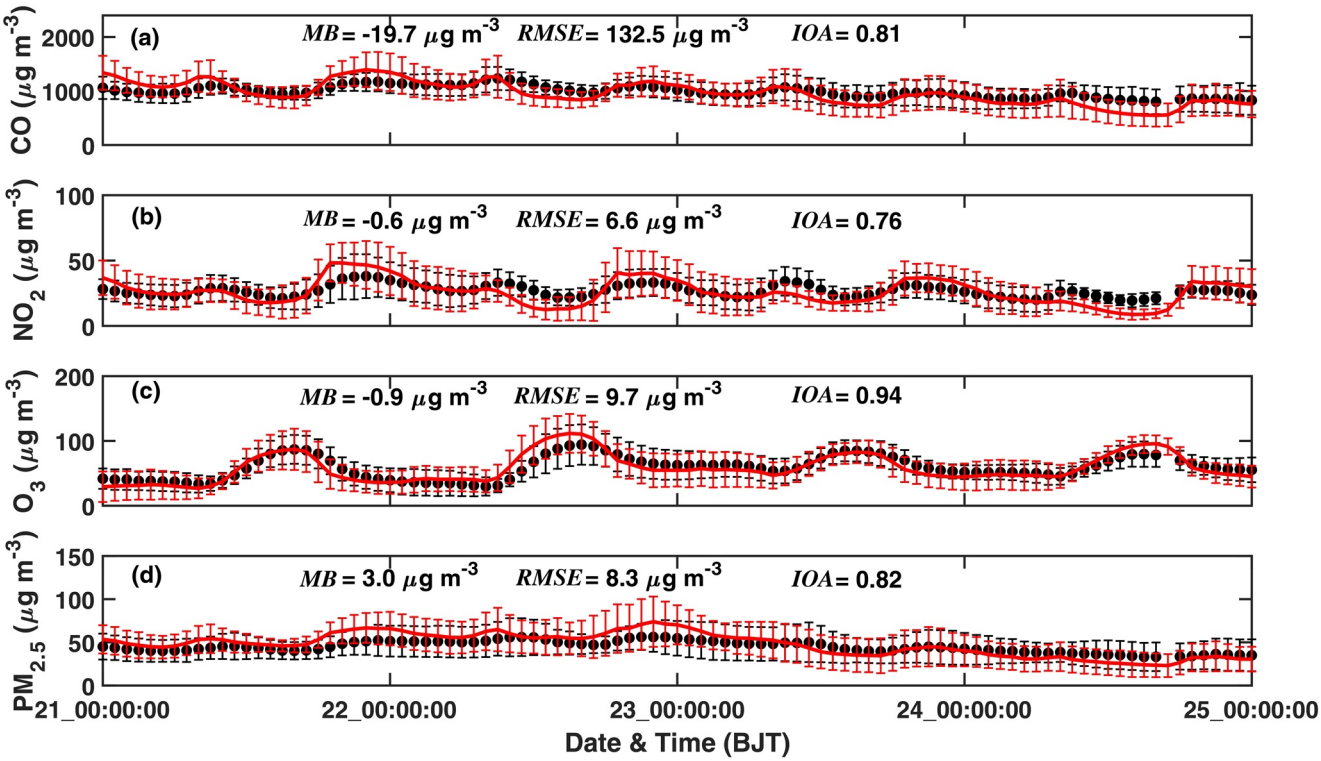

Figure 3. Comparison of observed (black dots) and simulated (solid red lines) diurnal profiles of near-surface hourly mass concentrations of (a) CO, (b) NO_2, (c) O_3, and (d) $PM_{2.5}$ averaged at monitoring sites in eight provinces of southern China from March 21 to 25, 2015. The error bars represent the standard deviation for the observation and simulation, respectively.

3.2. Impacts of BB-PSEA on Near-Surface $PM_{2.5}$ and O_3 Concentrations in Southern China

3.2.1. Effects of BB-PSEA on Near-Surface $PM_{2.5}$ and O_3 Concentrations

Figure 5 shows the total effect of BB-PSEA on near-surface CO, $PM_{2.5}$, and O_3 concentrations averaged from March 21 to March 25, 2015 by differentiating the BASE and BB0 experiments. The horizontal wind field at 850 hPa for the BASE case is overlaid on the spatial distribution of the $PM_{2.5}$ difference. CO is a good indicator for investigating the regional transport of BB-PSEA because of the large emissions from BB and long lifetime. Figure 5a indicates that BB-PSEA increases near-surface CO concentrations by more than

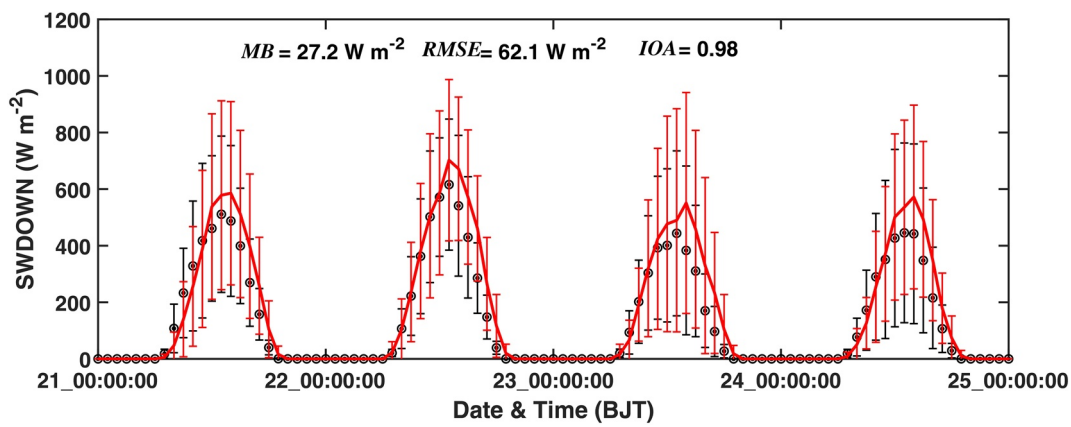

Figure 4. Comparison of observed (black dots) and simulated (red lines) SWDOWN averaged at the 15 observation sites in eight provinces of southern China from March 21 to 25, 2015. The error bars represent the standard deviation in the 15 sites for the observation and simulation, respectively.

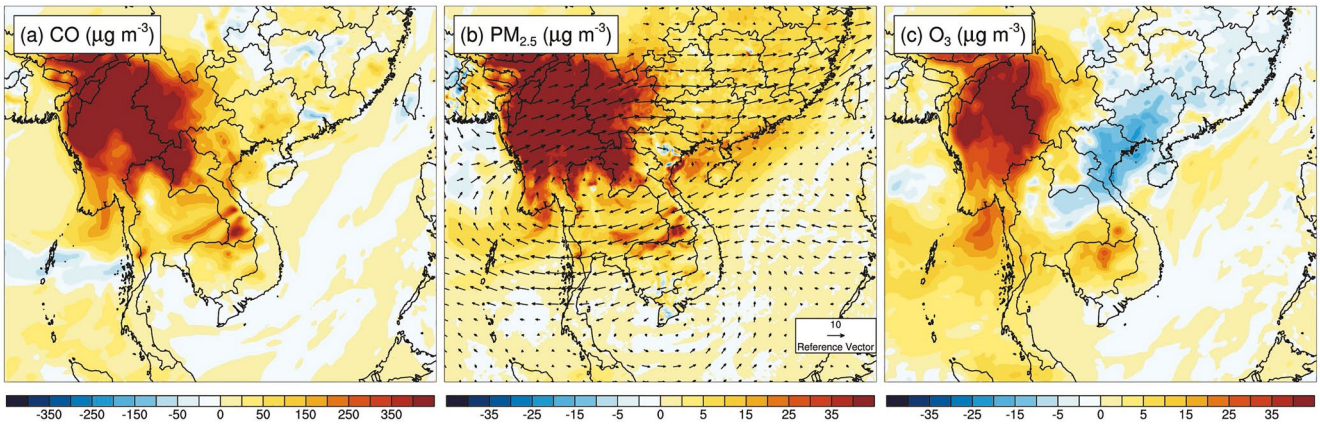

Figure 5. The total effects of BB-PSEA on near-surface (a) CO, (b) $PM_{2.5}$, and (c) O_3 concentrations averaged from March 21 to 25, 2015. The average wind field at 850 hPa from the BASE case is overlaid in (b).

300 μg m^{-3} in YNP and 0–50 μg m^{-3} in ODA, indicating the importance of BB-PSEA in air quality in southern China. On average, BB-PSEA increases CO concentrations by 296.2 μg m^{-3} (23.0%) in YNP and 20.2 μg m^{-3} (2.3%) in ODA. BB-PSEA increases near-surface $PM_{2.5}$ concentrations by more than 40 μg m^{-3} in the source region and YNP, which is adjacent to PSEA (Figure 5b). In ODA, near-surface $PM_{2.5}$ concentrations are increased by up to 25 μg m^{-3}, but they are slightly decreased by less than 5 μg m^{-3} in some regions. The average near-surface $PM_{2.5}$ contribution of emissions from BB-PSEA is 39.3 μg m^{-3} (68.0%) and 8.4 μg m^{-3} (24.1%) in YNP and ODA relative to the BASE case, respectively. The $PM_{2.5}$ enhancement in YNP is mainly contributed to primary organic aerosols (POAs) (32.7%), nitrate (24.5%), and unspecified species (25.1%). However, in ODA, nitrate, ammonium, and sulfate constitute the three most important species to the $PM_{2.5}$ enhancement, with the contribution of 60.8%, 21.1%, and 8.6%, respectively. The primary aerosols dominate the $PM_{2.5}$ enhancement in YNP, but the secondary aerosols become predominant in ODA.

BB-PSEA significantly enhances near-surface O_3 concentrations by over 40 μg m^{-3} in western YNP, but O_3 enhancement gradually decreases from the western to the eastern part of YNP (Figure 5c). In ODA, BB-PSEA generally inhibits O_3 photochemistry and only slightly enhances O_3 formation in some small regions. On average, BB-PSEA contributes to O_3 concentrations of 18.1 μg m^{-3} (19.4%) in YNP and decreases the O_3 concentrations in ODA by 3.7 μg m^{-3} (5.3%) relative to the BASE case. These results are consistent with the observed lower O_3 concentrations in the PRD under the influence of BB-PSEA (Deng et al., 2008) but are not in agreement with the simulations by Fu et al. (2012), who showed that BB-PSEA increases near-surface O_3 concentrations by 10%–30% in southern China, probably because of the absence of API and ARI effects in the CMAQ model. This will be discussed in the following sections.

BB plumes can be lifted above the PBL and transported to downwind areas along the westerly wind. BB-PSEA significantly increases CO concentrations by more than 300 μg m^{-3} from the surface to 4 km near the source region, and the enhancement is higher from 1.5 to 4 km in the downwind areas than that from the surface to 1.5 km. The $PM_{2.5}$ contributions of BB-PSEA are more than 60 μg m^{-3} from the surface to 3 km near the source region. In the downwind areas, the contribution is the most significant from 2 to 4 km, ranging from 16 to 36 μg m^{-3}, and is generally less than 12 μg m^{-3} in the PBL. O_3 concentrations are also increased by more than 60 μg m^{-3} from the surface to 3 km near the source region because of the numerous emissions of NO_x and VOCs from BB-PSEA. In the downwind areas, BB-PSEA increases O_3 concentrations by 12–28 μg m^{-3} from 2 to 4 km but decreases O_3 concentrations from the surface to 2 km, particularly near the surface level. This suggested that in addition to contributions of precursors from BB-PSEA, ARI and API induced by BB-PSEA also influence O_3 photochemistry.

Furthermore, all simulations are based on the source-oriented model (SOM), and therefore, in the BASE case, the $PM_{2.5}$ originated from BB-PSEA is marked. The direct $PM_{2.5}$ contribution of BB-PSEA is 34.8 μg m^{-3} (60.3%) and 4.7 μg m^{-3} (13.7%) in YNP and ODA relative to the BASE case, respectively, which differ from those evaluated by the BFM. The difference in $PM_{2.5}$ contributions between the BFM and SOM is likely

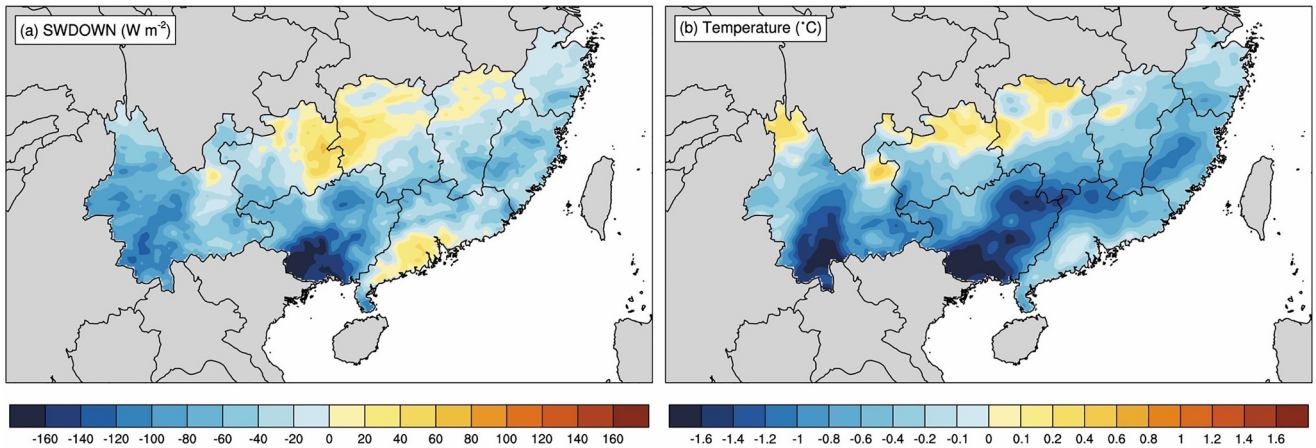

Figure 6. Spatial distribution of the average (a) SWDOWN and (b) surface temperature from March 21 to 25, 2015 due to the ARI effect of BB-PSEA.

because of the chemical interactions of local emissions with those from BB-PSEA and the ARI/API effects of BB-PSEA emissions.

3.2.2. Impacts of ARI and API From BB-PSEA on $PM_{2.5}$ Concentration and O_3 Formation

The ARI effects of BB-PSEA are calculated by differentiating the BASE and BB_ARI0 cases. Figure 6 shows that the daytime SWDOWN is reduced by up to 120 W m^{-2} in YNP and 160 W m^{-2} in ODA, decreasing the daytime near-surface temperature by more than 1.6°C in southern China. The larger decrease of SWDOWN in Guangxi Province of ODA compared to that in YNP is probably caused by the larger increase of cloud cover in Guangxi Province than in YNP (Figure S4c in Supporting Information S1). In addition, the ARI effects of BB-PSEA increase the temperature in the upper PBL by up to 0.8°C in YNP at 14:00 LT and 0.8°C in ODA at 18:00 LT (Figure S5 in Supporting Information S1). This is likely because of aerosols such as black and organic carbon in the BB plume absorbing solar radiation and heating the atmosphere in the upper PBL. Surface cooling and upper-level heating caused by BB have also been reported in previous studies (Ding et al., 2013; Li et al., 2018). The slight increase of SWDOWN and surface temperature in southern China might be caused by the reduced cloud cover due to changes in atmospheric stratification (Figure S4c in Supporting Information S1). On the regional and temporal averages from March 21 to March 25, 2015, the ARI effects of BB-PSEA attenuate the SWDOWN by 62.9 W m^{-2} (10.5%) and 31.5 W m^{-2} (8.9%) in YNP and ODA, respectively, relative to the BASE case, lowering the near-surface temperature by 0.6 and 0.5 °C, respectively, and reducing the PBLH by 83.1 m (9.8%) and 38.5 m (6.4%), respectively (Figure S5c in Supporting Information S1). The ARI effect of BB-PSEA on air quality in southern China is generally not significant or is uncertain. Figure 7 demonstrates the time series of simulated $PM_{2.5}$ and O_3 concentrations on the regional average in YNP and ODA from the BASE and BB_ARI0 cases. The ARI effect increases the mean $PM_{2.5}$ concentrations by 2.2 μg m^{-3} (4.0%) and 1.0 μg m^{-3} (2.9%) in YNP and ODA, respectively, but decreases the mean O_3 concentrations by 4.8 μg m^{-3} (4.9%) and 1.0 μg m^{-3} (1.4%), respectively. This is caused by the suppression of the vertical dispersion of air pollutants. It is well established that ARI suppresses the development of the PBL and facilitates the accumulation of air pollutants, deteriorating air quality (e.g., Gao et al., 2016; Li et al., 2020; Wang et al., 2014; X. Zhang et al., 2018). Figures S6b and S6e in Supporting Information S1 show that an anticyclone controls the PSEA and southern China during the simulation period. The ARI effect increases the temperature at 700 hPa (Figure S6a in Supporting Information S1) and decreases it at 850 hPa (Figure S6d in Supporting Information S1), altering the temperature stratification, lowering geopotential height in YNP and southern part of ODA, and raising geopotential height in the northern part of ODA (Figures S6c and S6f in Supporting Information S1). This results in cyclonic anomalies at 700 hPa and 850 hPa, and favors the anomalous convergence in the lower troposphere, leading to the increase in cloud cover in YNP and the southern part of ODA and the decrease in cloud cover in the northern part of ODA. The change of cloud cover correspondingly reduces or enhances the photolysis rate, and therefore affects O_3 concentrations in the corresponding areas (Figure S4 in Supporting Information

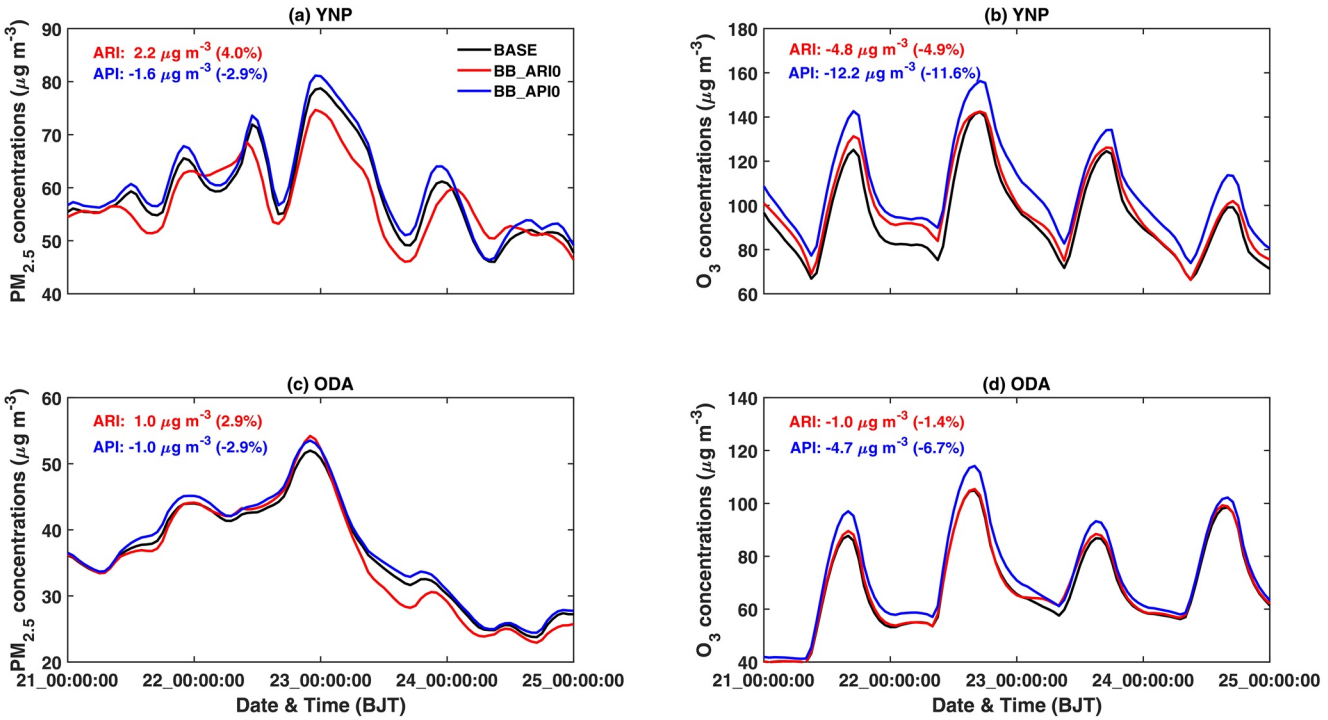

Figure 7. Time series of simulated $PM_{2.5}$ and O_3 concentrations on the regional average in YNP (a, b) and ODA (c, d) for the BASE (black lines), BB_ARI0 (red lines), and BB_API0 (blue lines) cases.

S1). Furthermore, decreased O_3 concentration in southern China due to the ARI effect may have originated from increased O_3 deposition due to a shallower PBL.

The API effect of BB-PSEA on photolysis rates is calculated as the difference between the BASE and BB_API0 experiments. The photolysis of NO_2 and O_3 to $O(^1d)$ plays an important role in the O_3 formation (Brasseur, 2003). Figure 8 indicates that the API effect of BB-PSEA significantly decreases the photolysis rates of NO_2 and O_3 to $O(^1d)$ by 3.2%–48.9% and 3.2%–54.8% in YNP, respectively, and 3.2%–53.0% and 4.0%–59.3% in ODA relative to the BASE case, respectively. The API effect decreases O_3 concentrations by up to 33.4 μg m^{-3} in YNP and 16.2 μg m^{-3} in ODA, respectively. On the daytime average, the API effect reduces the photolysis rates of NO_2 and O_3 to $O(^1d)$ by 26.5% and 30.3% in YNP, respectively, and 21.4% and 25.2% in ODA,

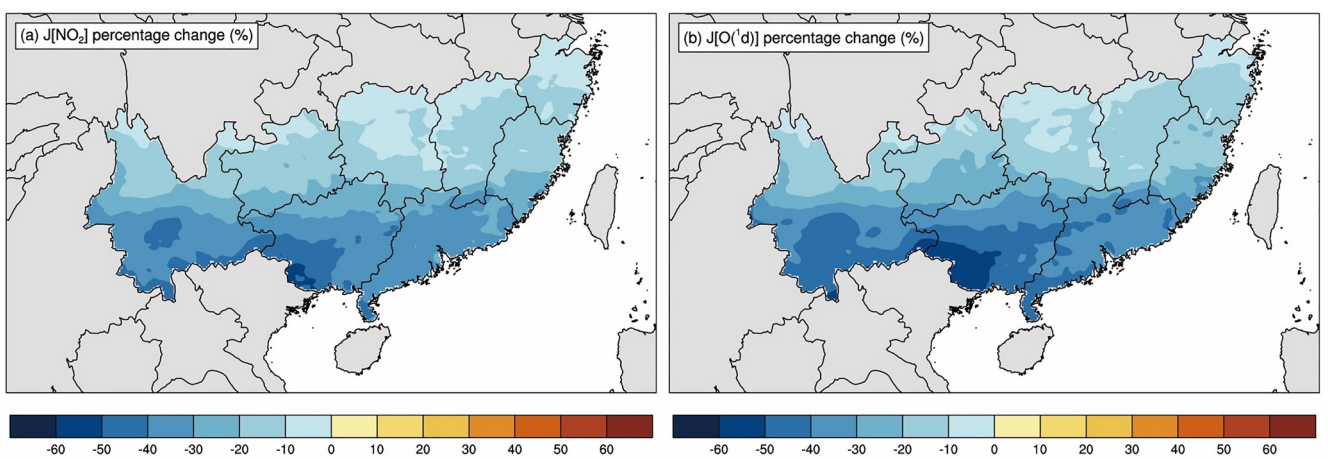

Figure 8. Spatial distributions of the average variation of (a) $J[NO_2]$ and (b) $J[O(^1d)]$ from March 21 to March 25, 2015 due to the API effect of BB-PSEA. $J[NO_2]$ and $J[O(^1d)]$ represent the photolysis rates of NO_2 and O_3 to $O(^1d)$, respectively.

Table 2
Contributions (μg m^{-3}) of Gaseous Emissions of BB-PSEA to Near-Surface O_3 and $PM_{2.5}$ Concentrations in YNP and ODA

	O_3	$PM_{2.5}$	Sulfate	Nitrate	Ammonium	SOA	POA	BC	Unspecified[a]
YNP	28.1	11.3	1.03	7.33	2.52	0.64	−0.09	−0.03	−0.08
ODA	−0.19	6.9	0.56	4.97	1.67	−0.04	−0.08	−0.05	−0.10

[a]Unspecified represents the unresolved primarily emitted aerosol species.

respectively. Correspondingly, the near-surface O_3 concentrations are reduced by 12.2 μg m^{-3} (11.6%) in YNP and 4.7 μg m^{-3} (6.7%) in ODA due to the API effect (Figure 7). The daily average OH concentrations in YNP and ODA are reduced by 25.2% and 22.3%, respectively, hindering the formation of secondary aerosols and further reducing $PM_{2.5}$ concentrations. The oxidation of VOCs and the aging of primary organics by OH constitute important secondary organic aerosol (SOA) formation pathways (Xing et al., 2019). Nitrate aerosols are formed from nitric acid to balance inorganic cations in the particle phase, which is determined by the NO_2 reaction with OH (homogeneous) and O_3 (heterogeneous) (Liu, Wu, et al., 2019). The gas-phase sulfate formation is dominated by OH and stabilized Criegee intermediates formed during the ozonolysis reaction of alkenes (G. Li et al., 2017; J. Li et al., 2017; M. Li et al., 2017; Liu, Bei, et al., 2019). The mean $PM_{2.5}$ concentrations in YNP and ODA decrease by 1.6 μg m^{-3} (2.9%) and 1.0 μg m^{-3} (2.9%), respectively, because of the API effects of BB-PSEA. This is mainly attributed to the reduction of nitrate aerosols.

The synergetic effect of both ARI and API from BB-PSEA is further evaluated by differentiating the BASE and BB_ARI&API0 experiments. On average, the synergetic effect slightly increases near-surface $PM_{2.5}$ concentrations, with $PM_{2.5}$ contributions of 1.5% in YNP and 0.2% in ODA relative to the BASE case. This is significantly lower than those caused only by the ARI of BB-PSEA. The present results are consistent with those of Wu et al. (2020), and indicates that the ARI effect considerably deteriorates particulate pollution during a heavy haze episode in the winter of the North China Plain, but the API effect substantially buffers the particulate pollution deterioration caused by ARI. Therefore, the difference in $PM_{2.5}$ contributions between the BFM and the SOM is not primarily caused by the ARI and API of BB-PSEA. Furthermore, the synergetic effect considerably hinders the O_3 formation in the lower PBL, reducing near-surface O_3 concentrations by 14.8% in YNP and 7.8% in ODA relative to the BASE case. However, based on the BFM evaluation, BB-PSEA increases near-surface O_3 concentrations by 19.4% in YNP, which is opposite to the contributions of the ARI or API or the synergetic effect, and decreases O_3 concentrations in ODA by 3.7 μg m^{-3} (5.3%), which is less than that caused by the synergetic effect.

3.2.3. Impacts of Gaseous Emissions From BB-PSEA on $PM_{2.5}$ and O_3 Concentrations

The impact of gaseous emissions from BB-PSEA on $PM_{2.5}$ concentration and O_3 formation in southern China is calculated as the difference between the BB_GAS and BB0 experiments. Figure S7 in Supporting Information S1 demonstrates that the CO concentrations for both the near surface and the vertical distributions are increased because of the gaseous emissions from BB-PSEA. The gaseous emissions from BB-PSEA increase near-surface O_3 concentrations by 28.1 μg m^{-3} in YNP, decrease O_3 concentrations by 0.19 μg m^{-3} in ODA (Table 2), and increase $PM_{2.5}$ concentrations by 11.3 and 6.9 μg m^{-3} in YNP and ODA, respectively (Table 2). Gaseous emissions influence O_3 photochemistry through two pathways: providing additional VOCs and NO_x and inducing ARI and API effect caused by the perturbation of aerosol concentrations. The present discussions reveal that the induced ARI and API effects generally reduce near-surface O_3 concentrations, and therefore, O_3 enhancement in YNP is mainly contributed by O_3 precursors from BB-PSEA. However, in ODA, increased O_3 levels are concentrated between 2 and 4 km and gradually become insignificant from 2 km to the surface level, showing a decreasing effect of O_3 precursors from BB-PSEA. This is caused by weakening westerly winds from 2 to 4 km to the surface level, as well as the short lifetime of NO_x and some VOCs (Figure S8a in Supporting Information S1). The slightly decreased near-surface O_3 concentrations in ODA may be attributed to the decrease in photolysis due to the API effect caused by $PM_{2.5}$ enhancement from the gaseous emissions from BB-PSEA, which reduces the NO_2 photolysis rate by 2.6%.

Increased $PM_{2.5}$ concentrations due to the gaseous emissions from BB-PSEA are predominantly contributed by the enhancement of nitrate aerosols, with a contribution of 64.8% in YNP and 71.6% in ODA relative

to the BB0 case. The enhancement of sulfate and ammonium aerosols accounts for 9.1% and 22.3% of the increased $PM_{2.5}$ concentrations in YNP, respectively, and 8.1% and 24.1% in ODA, respectively. Nitrate formation in the atmosphere is dependent on its precursors and atmospheric oxidation capacity (AOC), alkali gases or metal ion, and the sulfate in the particle phase. In YNP, which is adjacent to the source area, the precursor and AOC play an important role in nitrate enhancement near the surface level. However, in ODA, both factors do not significantly contribute to nitrate enhancement near the surface level, considering the decreased O_3 and rapid loss of NO_x in and near the source areas.

BB is the largest natural NH_3 source on land (Paulot et al., 2014), and it has been estimated to contribute 11%–23% of the global burden of NH_4NO_3 particles (Paulot et al., 2017). Therefore, NH_3 emitted by BB-PSEA might be the most important factor leading to an increase in nitrate levels in southern China. Chang et al. (2021) have shown that observed NH_3 concentrations display an urban (~30 μg m^{-3}) to suburban (~24 μg m^{-3}) to rural (~11 μg m^{-3}) gradient during March at nine sites in Chiang Mai, Thailand and BB contributes 21.0% of NH_3 concentrations in rural sites of Chiang Mai during March and April. The simulated NH_3 concentrations at the nine sites in Chiang Mai also show an urban (12.7 μg m^{-3}) to suburban (11.7 μg m^{-3}) to rural (9.5 μg m^{-3}) gradient, although the model underestimates the observed NH_3 concentrations. This may be caused by uncertainties in NH_3 emissions from nonagricultural activities, such as traffic, which is not included in the current emission inventories. The simulated near-surface NH_3 concentrations from BB emissions contribute 24.6% to the total NH_3 concentrations at the rural sites in Chiang Mai, which is comparable to the results from Chang et al. (2021). The emissions of BB-PSEA dominate the NH_3 level in YNP and ODA, with near-surface NH_3 contributions of 42.4% and 55.0%, respectively. The enhancement of NH_3 concentrations due to BB-PSEA emissions is significant from the surface level to approximately 4 km (Figure S8b in Supporting Information S1). Based on BB_GAS, a further sensitivity simulation is performed, wherein NH_3 emissions of BB-PSEA are excluded. A comparison with the BB0 experiment suggests that the nitrate concentration is enhanced by 2.1 and 0.12 μg m^{-3} in YNP and ODA, respectively. These values are significantly lower than those obtained by differentiating BB_GAS and BB0 (Table 2), and demonstrate that the NH_3 emissions from BB-PSEA play a key role in nitrate enhancement. Sulfate formation is generally determined by the heterogeneous and aqueous reactions of SO_2 in the atmosphere (G. Li et al., 2017; J. Li et al., 2017; M. Li et al., 2017; Liu, Bei, et al., 2019). The increase in sulfate concentration is mainly caused by the substantial increase in NH_3 concentration due to BB-PSEA, which not only provides high NH_3 conditions but also significantly enhances the nitrate and ammonium formation to facilitate the wet growth of aerosols and further SO_2 heterogeneous conversion. Therefore, NH_3 emissions from BB-PSEA play a key role in the formation of secondary inorganic aerosols, with $PM_{2.5}$ contribution of 7.6 and 7.0 μg m^{-3} in YNP and ODA, respectively. Almost all the enhancement of near-surface $PM_{2.5}$ concentrations in ODA is contributed by NH_3 emissions from BB-PSEA. Figures S7c and S7d in Supporting Information S1 demonstrate that nitrate and sulfate aerosols increase by up to 20 μg m^{-3} from the surface to 4 km, and the enhancements are higher from 2 to 4 km along the transport of BB plumes, with higher NH_3 emissions than those from the surface to 2 km. The gaseous emissions from BB-PSEA increase the near-surface SOA concentration by 5.6% in YNP, indicating the contribution of SOA precursors from BB-PSEA and AOC enhancement, but decrease the SOA level slightly in ODA, which might be caused by the decrease in O_3 formation.

4. Conclusions

The impact of emissions from BB-PSEA on $PM_{2.5}$ and O_3 concentrations in southern China is investigated by simulating an air pollution episode from March 21 to 25, 2015, using a source-oriented WRF-Chem model. The model separates the emissions from the BB-PSEA and other sources and can be used to evaluate the effects of ARI and API caused by emissions from BB-PSEA. Generally, the model performs well in simulating the spatial and temporal distribution of AOD, SWDOWN, $PM_{2.5}$, O_3, CO, and NO_2 concentrations during the simulation period.

The total effect of BB-PSEA increases near-surface $PM_{2.5}$ concentrations by 39.3 μg m^{-3} (68.0%) in YNP and 8.4 μg m^{-3} (24.1%) in ODA, indicating that BB-PSEA plays an important role in $PM_{2.5}$ pollution in southern China during springtime. The $PM_{2.5}$ increase in YNP is mainly caused by the enhancement of POA (32.7%), followed by unspecified species (25.1%) and nitrate (24.5%), while the $PM_{2.5}$ increase in ODA is dominated by the enhancement of secondary inorganic aerosols, including nitrate (60.8%), ammonium (21.1%), and

sulfate (8.6%). BB-PSEA increases near-surface O_3 concentrations by 18.1 μg m^{-3} (19.4%) in YNP and decreases O_3 concentrations in ODA by 3.7 μg m^{-3} (5.3%), which is consistent with the observations of Deng et al. (2008).

The ARI effect of BB-PSEA suppresses the development of PBL and facilitates the accumulation of air pollutants, increasing near-surface $PM_{2.5}$ concentrations by 2.2 μg m^{-3} in YNP and 1.0 μg m^{-3} in ODA. However, near-surface O_3 concentrations are decreased by 4.8 and 1.0 μg m^{-3} in YNP and ODA, respectively. The API effect significantly reduces the photolysis rates of NO_2 and O_3 to $O(^1d)$, reducing near-surface O_3 concentrations by 12.2 μg m^{-3} in YNP and 4.7 μg m^{-3} in ODA. In addition, the API effect decreases OH concentrations by 25.2% in YNP and 22.3% in ODA, which hinders the formation of secondary aerosols and further reduces $PM_{2.5}$ concentrations. The API effect of BB-PSEA reduces $PM_{2.5}$ concentrations by 1.6 μg m^{-3} in YNP and 1.0 μg m^{-3} in ODA. The synergetic effect of ARI and API slightly increases the near-surface $PM_{2.5}$ concentrations in southern China because of the buffer of API to the particulate pollution deterioration caused by ARI, but considerably reduces the near-surface O_3 concentrations both in YNP and ODA.

The gaseous emissions from BB-PSEA increase near-surface O_3 concentrations by 28.1 μg m^{-3} in YNP, but decrease O_3 concentrations by 0.19 μg m^{-3} in ODA. The remarkable O_3 increase in YNP is mainly caused by precursor emissions from BB-PSEA, whereas the O_3 decrease in ODA is likely attributed to the decrease in photolysis caused by $PM_{2.5}$ enhancement from the gaseous emissions from BB-PSEA. The gaseous emissions from BB-PSEA increase $PM_{2.5}$ concentrations by 11.3 μg m^{-3} in YNP and 6.9 μg m^{-3} in ODA, and the $PM_{2.5}$ increase is mainly caused by the enhancement of nitrate aerosols, with contributions of 64.8% in YNP and 71.6% in ODA. NH_3 emissions from BB-PSEA play a key role in nitrate enhancement in both YNP and ODA, and dominate the increased $PM_{2.5}$ concentration in ODA.

The results presented here from the model indicate that BB-PSEA is an important source for enhancing near-surface $PM_{2.5}$ concentrations in southern China and O_3 concentrations in YNP during springtime, although it reduces O_3 concentrations in ODA through the combined effects of ARI and API. NH_3 emissions from BB-PSEA play a key role in the enhancement of secondary inorganic aerosols in southern China.

The present findings are based on one case study, with the aim of providing a comprehensive evaluation of the effect of BB-PSEA on air quality in southern China. The impact of BB-PSEA may vary significantly because of the large variability in BB emissions and the atmospheric circulation. Therefore, further studies with longer time simulations are warranted to quantify the impact of BB-PSEA on air quality and climate in southern China.

Data Availability Statement

The hourly measurement data of $PM_{2.5}$, O_3, CO, and NO_2 in southern China, the hourly observed solar radiation data, and the model output can be accessed at Zenodo (https://zenodo.org/record/5348505#.YS864jgzYuU).

Acknowledgment
This study is supported by the Strategic Priority Research Program of the Chinese Academy of Sciences (No. XDB40030203), the National Natural Science Foundation of China (Nos. 41807310 and 41661144020), the Fundamental Research Funds for the Central Universities (No. GK202003066), and the Natural Science Foundation of Shaanxi Province (2020JQ-414).

References

Ajoku, O. F., Miller, A. J., & Norris, J. R. (2021). Impacts of aerosols produced by biomass burning on the stratocumulus-to-cumulus transition in the equatorial Atlantic. *Atmospheric Science Letters*, *22*, e1025. https://doi.org/10.1002/asl.1025

Binkowski, F. S., & Roselle, S. J. (2003). Models-3 community multiscale air quality (CMAQ) model aerosol component—1. Model description. *Journal of Geophysical Research: Atmospheres*, *108*(D6). https://doi.org/10.1029/2001jd001409

Bond, T. C., Streets, D. G., Yarber, K. F., Nelson, S. M., Woo, J. H., & Klimont, Z. (2004). A technology-based global inventory of black and organic carbon emissions from combustion. *Journal of Geophysical Research: Atmospheres*, *109*(D14), 43. https://doi.org/10.1029/2003jd003697

Booth, B. B. B., Dunstone, N. J., Halloran, P. R., Andrews, T., & Bellouin, N. (2012). Aerosols implicated as a prime driver of twentieth-century North Atlantic climate variability. *Nature*, *484*, 228–232. https://doi.org/10.1038/nature10946

Brasseur, G. P. (2003). *Atmospheric chemistry in a changing world: An integration and synthesis of a decade of tropospheric chemistry research: The International Global Atmospheric Chemistry Project of the International Geosphere-Biosphere Programme*. Springer.

Brasseur, G. P., Orlando, J. J., & Tyndall, G. S. (1999). *Atmospheric chemistry and the Earth system*. Oxford University Press.

Chang, Y. H., Zhang, Y. L., Kawichai, S., Wang, Q., Damme, M. V., Clarisse, L., et al. (2021). Convergent evidence for the pervasive but limited contribution of biomass burning to atmospheric ammonia in peninsular Southeast Asia. *Atmospheric Chemistry and Physics*, *21*, 7187–7198. https://doi.org/10.5194/acp-21-7187-2021

Chen, F., & Dudhia, J. (2001). Coupling an advanced land surface-hydrology model with the Penn State-NCAR MM5 modeling system. Part I: Model implementation and sensitivity. *Monthly Weather Review*, *129*(4), 569–585. https://doi.org/10.1175/1520-0493(2001)129<0569:caalsh>2.0.co;2

Chou, M. D., & Suarez, M. J. (1999). A solar radiation parameterization for atmospheric studies, NASA/ TM-1999-10460. NASA Technical Report.

Chou, M. D., Suarez, M. J., Liang, X. Z., Yan, M. H., & Cote, C. (2001). A thermal infrared radiation parameterization for atmospheric studies. NASA/TM-2001-104606.

Cui, M., Chen, Y., Zheng, M., Li, J., Tang, J., Han, Y., et al. (2018). Emissions and characteristics of particulate matter from rainforest burning in the Southeast Asia. *Atmospheric Environment*, *191*, 194–204. https://doi.org/10.1016/j.atmosenv.2018.07.062

Deng, X., Tie, X., Zhou, X., Wo, D., Zhong, L., Tan, H., et al. (2008). Effects of Southeast Asia biomass burning on aerosols and ozone concentrations over the Pearl River Delta (PRD) region. *Atmospheric Environment*, *42*(36), 8493–8501. https://doi.org/10.1016/j.atmosenv.2008.08.013

Ding, A. J., Fu, C. B., Yang, X. Q., Sun, J. N., Petaja, T., Kerminen, V. M., et al. (2013). Intense atmospheric pollution modifies weather: A case of mixed biomass burning with fossil fuel combustion pollution in eastern China. *Atmospheric Chemistry and Physics*, *13*(20), 10545–10554. https://doi.org/10.5194/acp-13-10545-2013

Fox, J., Fujita, Y., Ngidang, D., Peluso, N., Potter, L., Sakuntaladewi, N., et al. (2009). Policies, political-economy, and Swidden in Southeast Asia. *Human Ecology*, *37*(3), 305–322. https://doi.org/10.1007/s10745-009-9240-7

Fu, J. S., Hsu, N. C., Gao, Y., Huang, K., Li, C., Lin, N. H., & Tsay, S. C. (2012). Evaluating the influences of biomass burning during 2006 BASE-ASIA: A regional chemical transport modeling. *Atmospheric Chemistry and Physics*, *12*(9), 3837–3855. https://doi.org/10.5194/acp-12-3837-2012

Gao, M., Carmichael, G. R., Wang, Y., Saide, P. E., Yu, M., Xin, J., et al. (2016). Modeling study of the 2010 regional haze event in the North China Plain. *Atmospheric Chemistry and Physics*, *16*(3), 1673–1691. https://doi.org/10.5194/acp-16-1673-2016

Grell, G. A., Peckham, S. E., Schmitz, R., McKeen, S. A., Frost, G., Skamarock, W. C., & Eder, B. (2005). Fully coupled "online" chemistry within the WRF model. *Atmospheric Environment*, *39*(37), 6957–6975. https://doi.org/10.1016/j.atmosenv.2005.04.027

Guenther, A., Karl, T., Harley, P., Wiedinmyer, C., Palmer, P. I., & Geron, C. (2006). Estimates of global terrestrial isoprene emissions using MEGAN (Model of Emissions of Gases and Aerosols from Nature). *Atmospheric Chemistry and Physics*, *6*, 3181–3210. https://doi.org/10.5194/acp-6-3181-2006

Guo, J., Deng, M., Lee, S. S., Wang, F., Li, Z., Zhai, P., et al. (2016). Delaying precipitation and lightning by air pollution over the Pearl River Delta. Part I: Observational analyses. *Journal of Geophysical Research: Atmospheres*, *121*, 6472–6488. https://doi.org/10.1002/2015JD023257

Hong, S.-Y., & Lim, J.-O. J. (2006). The WRF Single-Moment 6-Class Microphysics Scheme (WSM6). *Asia-Pacific Journal of Atmospheric Sciences*, *42*(2), 129–151.

Horowitz, L. W., Walters, S., Mauzerall, D. L., Emmons, L. K., Rasch, P. J., Granier, C., et al. (2003). A global simulation of tropospheric ozone and related tracers: Description and evaluation of MOZART, version 2. *Journal of Geophysical Research: Atmospheres*, *108*(D24), 4784. https://doi.org/10.1029/2002jd002853

Janjić, Z. I. (2002). *Nonsingular implementation of the Mellor-Yamada Level 2.5 Scheme in the NCEP Meso Model*.

Jian, Y., & Fu, T. M. (2014). Injection heights of springtime biomass-burning plumes over peninsular Southeast Asia and their impacts on long-range pollutant transport. *Atmospheric Chemistry and Physics*, *14*(8), 3977–3989. https://doi.org/10.5194/acp-14-3977-2014

Jiang, X., Wiedinmyer, C., & Carlton, A. G. (2012). Aerosols from Fires: An examination of the effects on ozone photochemistry in the Western United States. *Environmental Science & Technology*, *46*(21), 11878–11886. https://doi.org/10.1021/es301541k

Levy, R., Hsu, C., Sayer, A., Mattoo, S., & Lee, J. (2017). *MODIS atmosphere L2 aerosol product. NASA MODIS adaptive processing system*. Goddard Space Flight Center. https://doi.org/10.5067/MODIS/MOD04_L2.061

Li, G., Bei, N., Cao, J., Huang, R., Wu, J., Feng, T., et al. (2017). A possible pathway for rapid growth of sulfate during haze days in China. *Atmospheric Chemistry and Physics*, *17*(5), 3301–3316. https://doi.org/10.5194/acp-17-3301-2017

Li, G., Bei, N., Tie, X., & Molina, L. T. (2011). Aerosol effects on the photochemistry in Mexico City during MCMA-2006/MILAGRO campaign. *Atmospheric Chemistry and Physics*, *11*(11), 5169–5182. https://doi.org/10.5194/acp-11-5169-2011

Li, G., Lei, W., Bei, N., & Molina, L. T. (2012). Contribution of garbage burning to chloride and PM2.5 in Mexico City. *Atmospheric Chemistry and Physics*, *12*(18), 8751–8761. https://doi.org/10.5194/acp-12-8751-2012

Li, G., Lei, W., Zavala, M., Volkamer, R., Dusanter, S., Stevens, P., & Molina, L. T. (2010). Impacts of HONO sources on the photochemistry in Mexico City during the MCMA-2006/MILAGO Campaign. *Atmospheric Chemistry and Physics*, *10*(14), 6551–6567. https://doi.org/10.5194/acp-10-6551-2010

Li, G., Zavala, M., Lei, W., Tsimpidi, A. P., Karydis, V. A., Pandis, S. N., et al. (2011). Simulations of organic aerosol concentrations in Mexico City using the WRF-CHEM model during the MCMA-2006/MILAGRO campaign. *Atmospheric Chemistry and Physics*, *11*(8), 3789–3809. https://doi.org/10.5194/acp-11-3789-2011

Li, G. H., Zhang, R. Y., Fan, J. W., & Tie, X. X. (2005). Impacts of black carbon aerosol on photolysis and ozone. *Journal of Geophysical Research: Atmospheres*, *110*(D23). https://doi.org/10.1029/2005jd005898

Li, J., Zhang, Y., Wang, Z., Sun, Y., Fu, P., Yang, Y., et al. (2017). Regional impact of biomass burning in Southeast Asia on atmospheric aerosols during the 2013 Seven South-East Asian Studies Project. *Aerosol and Air Quality Research*, *17*(12), 2924–2941. https://doi.org/10.4209/aaqr.2016.09.0422

Li, J. W., Han, Z. W., Wu, Y. F., Xiong, Z., Xia, X. G., Li, J., et al. (2020). Aerosol radiative effects and feedbacks on boundary layer meteorology and $PM_{2.5}$ chemical components during winter haze events over the Beijing-Tianjin-Hebei region. *Atmospheric Chemistry and Physics*, *20*(14), 8659–8690. https://doi.org/10.5194/acp-20-8659-2020

Li, M., Wang, T., Xie, M., Li, S., Zhuang, B., Chen, P., et al. (2018). Agricultural fire impacts on ozone photochemistry over the Yangtze River Delta Region, East China. *Journal of Geophysical Research: Atmospheres*, *123*(12), 6605–6623. https://doi.org/10.1029/2018jd028582

Li, M., Zhang, Q., Kurokawa, J.-i., Woo, J.-H., He, K., Lu, Z., et al. (2017). MIX: A mosaic Asian anthropogenic emission inventory under the international collaboration framework of the MICS-Asia and HTAP. *Atmospheric Chemistry and Physics*, *17*(2), 935–963. https://doi.org/10.5194/acp-17-935-2017

Li, Z., Lau, W. K.-M., Ramanathan, V., Wu, G., Ding, Y., Monoj, M. G., et al. (2016). Aerosol and monsoon climate interactions over Asia. *Reviews of Geophysics*, *54*(4), 866–929. https://doi.org/10.1002/2015RG000500

Liu, L., Bei, N., Wu, J., Liu, S., Zhou, J., Li, X., et al. (2019). Effects of stabilized Criegee intermediates (sCIs) on sulfate formation: A sensitivity analysis during summertime in Beijing-Tianjin-Hebei (BTH), China. *Atmospheric Chemistry and Physics*, *19*(20), 13341–13354. https://doi.org/10.5194/acp-19-13341-2019

Liu, L., Cheng, Y., Wang, S., Wei, C., Pöhlker, M. L., Pöhlker, C., et al. (2020). Impact of biomass burning aerosols on radiation, clouds, and precipitation over the Amazon: Relative importance of aerosol-cloud and aerosol-radiation interactions. *Atmospheric Chemistry and Physics*, *20*, 13283–13301. https://doi.org/10.5194/acp-20-13283-2020

Liu, L., Wu, J., Liu, S., Li, X., Zhou, J., Feng, T., et al. (2019). Effects of organic coating on the nitrate formation by suppressing the N_2O_5 heterogeneous hydrolysis: A case study during wintertime in Beijing-Tianjin-Hebei (BTH). *Atmospheric Chemistry and Physics*, *19*(12), 8189–8207. https://doi.org/10.5194/acp-19-8189-2019

Liu, T., Mickley, L. J., Marlier, M. E., DeFries, R. S., Khan, M. F., Latif, M. T., & Karambelas, A. (2020). Diagnosing spatial biases and uncertainties in global fire emissions inventories: Indonesia as regional case study. *Remote Sensing of Environment*, *237*, 111557. https://doi.org/10.1016/j.rse.2019.111557

Marmur, A., Unal, A., Mulholland, J. A., & Russell, A. G. (2005). Optimization-based source apportionment of $PM_{2.5}$ incorporating gas-to-particle ratios. *Environmental Science & Technology*, *39*(9), 3245–3254. https://doi.org/10.1021/es0490121

Nenes, A., Pandis, S. N., & Pilinis, C. (1998). ISORROPIA: A new thermodynamic equilibrium model for multiphase multicomponent inorganic aerosols. *Aquatic Geochemistry*, *4*(1), 123–152. https://doi.org/10.1023/a:1009604003981

Paulot, F., Jacob, D. J., Pinder, R. W., Bash, J. O., Travis, K., & Henze, D. K. (2014). Ammonia emissions in the United States, European Union, and China derived by high-resolution inversion of ammonium wet deposition data: Interpretation with a new agricultural emissions inventory (MASAGE_NH3). *Journal of Geophysical Research: Atmospheres*, *119*(7), 4343–4364. https://doi.org/10.1002/2013jd021130

Paulot, F., Paynter, D., Ginoux, P., Naik, V., Whitburn, S., Van Damme, M., et al. (2017). Gas-aerosol partitioning of ammonia in biomass burning plumes: Implications for the interpretation of spaceborne observations of ammonia and the radiative forcing of ammonium nitrate. *Geophysical Research Letters*, *44*(15), 8084–8093. https://doi.org/10.1002/2017gl074215

Suepa, T., Qi, J., Lawawirojwong, S., & Messina, J. P. (2016). Understanding spatio-temporal variation of vegetation phenology and rainfall seasonality in the monsoon Southeast Asia. *Environmental Research*, *147*, 621–629. https://doi.org/10.1016/j.envres.2016.02.005

Tie, X. X., Madronich, S., Walters, S., Zhang, R. Y., Rasch, P., & Collins, W. (2003). Effect of clouds on photolysis and oxidants in the troposphere. *Journal of Geophysical Research: Atmospheres*, *108*(D20). https://doi.org/10.1029/2003jd003659

Wang, Y., Zhang, Y., Hao, J., & Luo, M. (2011). Seasonal and spatial variability of surface ozone over China: Contributions from background and domestic pollution. *Atmospheric Chemistry and Physics*, *11*, 3511–3525. https://doi.org/10.5194/acp-11-3511-2011

Wang, Z. F., Li, J., Wang, Z., Yang, W. Y., Tang, X., Ge, B. Z., et al. (2014). Modeling study of regional severe hazes over mid-eastern China in January 2013 and its implications on pollution prevention and control. *Science China Earth Sciences*, *57*(1), 3–13. https://doi.org/10.1007/s11430-013-4793-0

Wesely, M. L. (1989). Parameterization of surface resistances to gaseous dry deposition in regional-scale numerical models. *Atmospheric Environment*, *23*(6), 1293–1304. https://doi.org/10.1016/0004-6981(89)90153-4

Wiedinmyer, C., Akagi, S. K., Yokelson, R. J., Emmons, L. K., Al-Saadi, J. A., Orlando, J. J., & Soja, A. J. (2011). The fire inventory from NCAR (FINN): A high resolution global model to estimate the emissions from open burning. *Geoscientific Model Development*, *4*(3), 625–641. https://doi.org/10.5194/gmd-4-625-2011

Wiedinmyer, C., Quayle, B., Geron, C., Belote, A., McKenzie, D., Zhang, X., et al. (2006). Estimating emissions from fires in North America for air quality modeling. *Atmospheric Environment*, *40*(19), 3419–3432. https://doi.org/10.1016/j.atmosenv.2006.02.010

Wu, J., Bei, N., Hu, B., Liu, S., Wang, Y., Shen, Z., et al. (2020). Aerosol-photolysis interaction reduces particulate matter during wintertime haze events. *Proceedings of the National Academy of Sciences of the United States of America*, *117*(18), 9755–9761. https://doi.org/10.1073/pnas.1916775117

Wu, J., Bei, N., Hu, B., Liu, S., Zhou, M., Wang, Q., et al. (2019). Aerosol-radiation feedback deteriorates the wintertime haze in the North China Plain. *Atmospheric Chemistry and Physics*, *19*(13), 8703–8719. https://doi.org/10.5194/acp-19-8703-2019

Xing, L., Wu, J., Elser, M., Tong, S., Liu, S., Li, X., et al. (2019). Wintertime secondary organic aerosol formation in Beijing-Tianjin-Hebei (BTH): Contributions of HONO sources and heterogeneous reactions. *Atmospheric Chemistry and Physics*, *19*(4), 2343–2359. https://doi.org/10.5194/acp-19-2343-2019

Zhang, H., & Ying, Q. (2011). Secondary organic aerosol formation and source apportionment in Southeast Texas. *Atmospheric Environment*, *45*(19), 3217–3227. https://doi.org/10.1016/j.atmosenv.2011.03.046

Zhang, L., Jacob, D. J., Yue, X., Downey, N. V., Wood, D. A., & Blewitt, D. (2014). Sources contributing to background surface ozone in the US Intermountain West. *Atmospheric Chemistry and Physics*, *14*(11), 5295–5309. https://doi.org/10.5194/acp-14-5295-2014

Zhang, X., Zhang, Q., Hong, C. P., Zheng, Y. X., Geng, G. N., Tong, D., et al. (2018). Enhancement of $PM_{2.5}$ concentrations by aerosol-meteorology interactions over China. *Journal of Geophysical Research: Atmospheres*, *123*(2), 1179–1194. https://doi.org/10.1002/2017jd027524

Zheng, B., Tong, D., Li, M., Liu, F., Hong, C. P., Geng, G. N., et al. (2018). Trends in China's anthropogenic emissions since 2010 as the consequence of clean air actions. *Atmospheric Chemistry and Physics*, *18*, 14095–14111. https://doi.org/10.5194/acp-18-14095-2018

Zhu, J., Xia, X., Che, H., Wang, J., Zhang, J., & Duan, Y. (2016). Study of aerosol optical properties at Kunming in Southwest China and long-range transport of biomass burning aerosols from North Burma. *Atmospheric Research*, *169*, 237–247. https://doi.org/10.1016/j.atmosres.2015.10.012

Zhu, J., Xia, X., Wang, J., Zhang, J., Wiedinmyer, C., Fisher, J. A., & Keller, C. A. (2017). Impact of Southeast Asian smoke on aerosol properties in Southwest China: First comparison of model simulations with satellite and ground observations. *Journal of Geophysical Research: Atmospheres*, *122*(7), 3904–3919. https://doi.org/10.1002/2016jd025793

Zhu, L., Martin, M. V., Gatti, L. V., Kahn, R., Hecobian, A., & Fischer, E. V. (2018). Development and implementation of a new biomass burning emissions injection height scheme (BBEIH v1.0) for the GEOS-Chem model (v9-01-01). *Geoscientific Model Development*, *11*(10), 4103–4116. https://doi.org/10.5194/gmd-11-4103-2018